Journal of Materials Chemistry C

ROYAL SOCIETY OF CHEMISTRY

PAPER

View Article Online
View Journal

Cite this: DOI: 10.1039/d5tc04105h

Structural phase transition and distortion-mode evolution in the one-dimensional [$CuBr_4$] chain structure of $RbCu_2Br_3$

Yousra Chakroun,[ab] Wajdi Cherif,[c] Carlos A. López,[ad] Lilia Ktari,[b] Brenda Martinelli,[e] Javier Gainza,[g] F. Serrano-Sánchez,[a] Mateus M. Ferrer,[e] Carlos Pecharromán,[a] José Luis Martínez,[a] María Teresa Fernández-Díaz,[f] João Elias F. S. Rodrigues*[ag] and José Antonio Alonso*[a]

The all-inorganic halide compound $RbCu_2Br_3$ represents a rare example of a 1D Cu(I)-based perovskite-derived architecture, yet its structural stability, phase evolution, and lattice dynamical behaviour remain largely unexplored. Here, we combine mechanochemical synthesis, high-resolution synchrotron and neutron powder diffraction, calorimetry, optical spectroscopies, and first-principles modelling to establish a complete structure–property framework for this compound. We show that ball milling yields highly crystalline $RbCu_2Br_3$ with the expected *Cmcm* structure at ambient conditions, built from double chains of edge-sharing [$CuBr_4$] tetrahedral units. Temperature-dependent diffraction and calorimetry reveal a previously unresolved continuous and reversible structural phase transition to a *Pnma* phase below ~250 K, driven by subtle cooperative tilting of the [$CuBr_4$] chains. Symmetry-mode analysis identifies two primary irreducible representations dominating the distortion energy landscape, clarifying the microscopic mechanism of symmetry breaking. Infrared spectroscopy uncovers an unusually large number of phonon modes, consistent with local symmetry lowering and weakly ionic Cu–Br bonds, while diffuse-reflectance measurements reveal both direct and indirect electronic transitions, consistent with DFT electronic-structure calculations. These results establish $RbCu_2Br_3$ as a structurally versatile, low-symmetry Cu(I) halide with an intrinsic propensity for lattice distortions coupled to its low-dimensional electronic structure, providing a foundation for future exploration of copper-based, lead-free perovskite alternatives.

Received 19th November 2025,
Accepted 29th January 2026

DOI: 10.1039/d5tc04105h

rsc.li/materials-c

1. Introduction

All-inorganic metal-halide perovskites are a remarkable group of materials known for their superior optoelectronic characteristics. These features include an exceptional charge-carrier mobility, extensive diffusion lengths, and short charge-relaxation times, making them attractive for high-efficiency energy conversion and diverse electronic applications.[1–6] Recently, these properties have sparked significant interest in deploying metal-halide perovskites beyond traditional photovoltaic applications. They are now being explored for uses such as photodetection,[7–9] photocatalysis,[10–12] laser technologies,[13,14] X-ray detection,[15–17] and solid-state batteries.[18]

Although metal-halide perovskites like $CsPbI_3$[19,20] or $CsPbBr_3$[21,22] boast impressive properties, their practical use is obstructed by the difficulty of developing synthesis methods that consistently yield stable compositions, ideal morphologies, and high-purity materials. In addition, environmental concerns, particularly the potential toxicity and ecological risks associated with lead, have become a major issue.[23,24] This has driven the search for lead-free alternatives, with tin-based perovskites emerging as a promising option.[25] The structural versatility of perovskites allows for the substitution of different atoms at the A, B, and X sites within the ABX_3 framework, offering opportunities to replace toxic elements like lead with less harmful metals, such as bismuth (Bi) and antimony (Sb).[26–28] Other options involve transition metal elements like copper (Cu).[29,30] Not only divalent, but also monovalent copper can be incorporated into the

[a] Instituto de Ciencia de Materiales de Madrid, CSIC, Cantoblanco, 28049 Madrid, Spain. E-mail: ja.alonso@icmm.csic.es, rodrigues.joaoelias@gmail.com
[b] Laboratory of Inorganic Chemistry, Faculty of Sciences of Sfax, University of Sfax, 3000 Sfax, Tunisia
[c] National Engineering School of Sfax (ENIS), Laboratory of Electromechanical Systems (LASEM), B.P.W. 3038, Sfax, Tunisia
[d] Instituto de Investigaciones en Tecnología Química (UNSL-CONICET) and Facultad de Química, Bioquímica y Farmacia, Almirante Brown 1455 (5700), San Luis, Argentina
[e] CCAF, PPGCEM/CDTec, Federal University of Pelotas, 96010-610 Pelotas, Rio Grande do Sul, Brazil
[f] Institut Laue Langevin, 38042 Grenoble Cedex, France
[g] ESRF – European Synchrotron Radiation Facility, 38000 Grenoble, France

perovskite halide framework. This is the case of the largely unexplored $RbCu_2Br_3$, or rubidium dicopper(I) bromide. It is an intriguing material with a unique set of properties.[31–33] This compound crystallizes in an orthorhombic structure with the space-group *Cmcm*. It has a band gap of approximately 1.64 eV (~780 nm), making it a potential candidate for optoelectronic applications. It presents an unusual 1D crystal structure, consisting of double chains of $[CuBr_4]$ tetrahedral units along the *c* direction; the transport path located in these double chains conforms to a 1D electronic structure.[31] The potential applications of $RbCu_2Br_3$ extend beyond traditional applications, with researchers exploring their use in X-ray detection, solid-state batteries, and other optoelectronic devices: one of the most fascinating aspects of $RbCu_2Br_3$ is related to its luminescence properties. As the temperature decreases, the crystals exhibit a transition from blue to orange light, which is attributed to the breaking of crystal symmetry due to thermally induced local deviations of the crystal field, resulting in a structural transition from the *Cmcm* to *Pnma* phase with low symmetry.[32] The crystals show double exciton radiative recombination of photoluminescence and radioluminescence at low temperatures. This property makes it a subject of interest for studies on photoluminescence and radioluminescence.

In this work, we establish a full structure–property framework for the low-dimensional Cu(I) halide $RbCu_2Br_3$. Mechanochemical synthesis yields phase-pure crystalline material adopting the orthorhombic *Cmcm* structure built from double $[CuBr_4]$ chains. High-resolution synchrotron and neutron diffraction reveal a continuous *Pnma* → *Cmcm* transition below ~250 K, arising from a cooperative chain-tilting instability. Symmetry-mode analysis identifies a small set of dominant irreducible representations that govern the symmetry lowering, providing a microscopic description of the distortion pathway. Infrared spectroscopy exposes a vibrational spectrum far richer than expected for the high-symmetry structure, consistent with local symmetry breaking and weakly ionic Cu–Br bonding. Optical diffuse reflectance, supported by DFT, shows the coexistence of direct and indirect electronic transitions. These combined results demonstrate that $RbCu_2Br_3$ is a highly distortion-responsive Cu(I) halide, where subtle lattice instabilities play a central role in shaping its vibrational and electronic behaviour.

2. Materials and methods

2.1. Synthesis

$RbCu_2Br_3$ was synthesized in polycrystalline powder form by mechano-chemical synthesis using a planetary ball mill from stoichiometric amounts of RbBr and CuBr. The total mass of reactants was 1 g, which was weighed and mixed with 20 zirconia balls (5 mm diameter) in a N_2-filled glove box. The reaction took place in a Retsch PM100 mill for 3 h at 450 rpm, in a sealed zirconia-lined jar with N_2 atmosphere.

2.2. Structural analysis

Bruker D5 diffractometer with Cu-Kα (λ = 1.5418 Å) radiation was used to collect a laboratory XRD pattern at room temperature. The crystallographic structure was studied by neutron powder diffraction (NPD) in D2B, a high-resolution two-axis diffractometer at the Institut Laue-Langevin (ILL) in Grenoble, France. The NPD patterns were collected at room temperature (298 K) with a wavelength of λ = 1.594 Å. The sample was contained in a cylindrical vanadium holder of 6 mm in diameter. The neutron scattering lengths for Rb, Cu, and Br are 7.09, 7.718, and 6.795, respectively. The thermal evolution of the crystallographic structure was studied by SXRD in the 100–530 K temperature range. The low-temperature patterns (100, 150, 200, and 250 K) were collected at the ID22 diffractometer[34] in the ESRF (Grenoble, France) with λ = 0.354 Å (35.0 keV). The patterns above room temperature were collected sequentially from 303 K up to 530 K, with intervals around 10 K, in high-angular resolution mode (multi-analyser detector set-up) on the MSPD diffractometer[35] in CELLS-ALBA Synchrotron in Cerdanyola del Valles (Spain), selecting an incident beam with 28 keV energy (λ = 0.44367 Å). The sample was contained in a 0.5 mm diameter quartz capillary that was rotating during the data acquisition. The NPD and SXRD data were analysed with the Rietveld method using the FullProf program.[36]

2.3. Calorimetric and morphological analyses

Thermogravimetry (TG) and differential scanning calorimetry (DSC) measurements were carried out in the range 130 to 520 K in a Mettler TA3000 system equipped with a DSC30 unit. The heating and cooling rates were 10 K min^{-1}, using about 70 mg of sample in each run, following the protocol in ref. 37. Field-Effect Scanning Electron Microscopy (FE-SEM) images were obtained in a FEI Nova microscope, with an acceleration potential of 5 kV, coupled to an energy-dispersive X-ray spectrometer (EDXS), working with an acceleration voltage of 18 kV and 60 s of acquisition time.

2.4. Reflectance and photoluminescence UV-vis and infrared reflectance spectroscopies

A UV-vis spectrophotometer, Jasco V660, attached with an integrating sphere, was employed to measure the optical diffuse reflectance spectrum at room temperature. Photoluminescence spectra were taken with a FluoroMax®-3 fluorometer from Horiba Jobin-Yvon using dense pellets. Far-infrared spectra at room temperature were collected using a Bruker Vertex 70V FTIR spectrophotometer equipped with an extended-range beam splitter, a Globar source, and a DTGS detector. Dense pellets were prepared by cold-press sintering in an optically polished zirconia die. The samples were measured in near-normal incidence using a reflectance accessory.

2.5. Density functional theory

Density Functional Theory (DFT) calculations for the compound $RbCu_2Br_3$ were performed using the CRYSTAL17 software package,[38] which employs a local Gaussian-type orbital (GTO) basis set. The exchange–correlation effects were modelled using the Perdew–Burke–Ernzerhof (PBE) generalized gradient approximation (GGA) functional.[39] All the atomic species, rubidium (Rb), copper (Cu), and bromine (Br) were described with triple-zeta valence basis sets augmented with polarization functions (POB-TZVP), as developed by Laun *et al.*[40] This basis set is optimized

for solid-state calculations and provides a high level of accuracy for electronic structure calculations of materials containing transition metals. The truncation of the infinite Coulomb and Hartree–Fock exchange series was controlled by defining five tolerance factors (a_k, k = 1–5) with values set to (8, 8, 8, 8, 16). These parameters govern the precision for evaluating overlap integrals, Coulomb integral penetration, exchange overlap, and pseudo-overlap in the exchange series. Sampling of the reciprocal space was conducted using a Pack–Monkhorst k-point grid with shrinking factors of 8 × 8 × 8. Integration over the Brillouin zone was performed using the Gilat net method to ensure numerical stability and convergence of electronic properties.

3. Results

3.1. Initial characterization

The high purity of $RbCu_2Br_3$ was initially assessed from laboratory powder XRD measurement at room temperature. The polycrystalline powder sample presents an orthorhombic symmetry defined in the space-group *Cmcm* (no. 63), in agreement with the scarce previous results of this phase.[31–33] The Rietveld refinement from laboratory XRD data is displayed in Fig. 1, providing a preliminary crystallographic structural model with unit-cell parameters: a = 9.8565(8) Å, b = 12.412(1) Å, and c = 5.5519(5) Å.

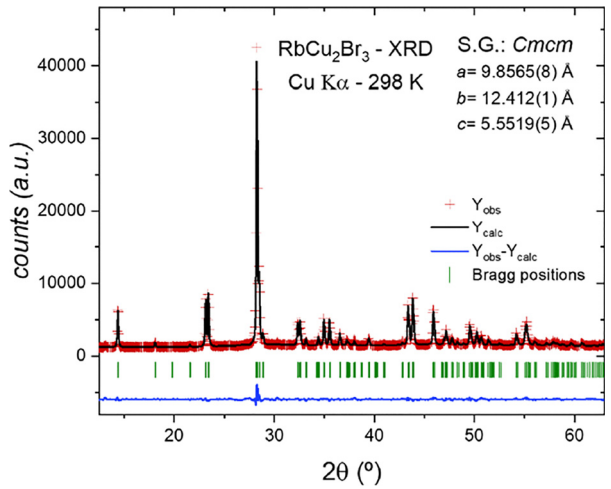

Fig. 1 Rietveld refinement from laboratory XRD pattern at room temperature. Rietveld plot: observed (red cross) and calculated (black line) X-ray diffraction pattern. Blue lines represent the fit residuals, and the green bars are the expected Bragg reflections.

The thermal stability was studied from TG and DSC measurements, as depicted in Fig. 2. In the TG curve (Fig. 2a), no anomalies are found until the decomposition onset of the sample at 500 K. The DSC curves (Fig. 2b) exhibit broad endothermic and exothermic peaks at *c.a.* 245–228 K for the heating and cooling runs, respectively. One can also see a ∼30 K hysteresis. This suggests the presence of a structural transition in this temperature range, which is evaluated in detail from temperature-dependent SXRD data, described below.

3.2. Morphological results

The FE-SEM images, exhibited in Fig. 3, offer detailed insights into the microstructure of the product synthesized *via* ball milling. At a lower magnification (30 000×), the sample is formed by irregularly shaped clusters comprising particles of varying sizes (Fig. 3a). Upon increasing the magnification to 60 000× (Fig. 3b and c), these clusters are revealed to consist of compact microparticles with sharp edges, typically ranging from 0.2 to 0.5 μm in size, combined with much larger microcrystals with dimensions superior to ∼1 μm. Remarkably, this high crystallite size was formed during the ball milling process. Elemental analysis using EDXS, in conjunction with the FE-SEM images, suggests an atomic ratio of approximately 1 : 2 : 3 for Rb : Cu : Br. A representative EDXS spectrum is provided in Fig. S1 of the SI, and additional SEM images can be found in Fig. S2.

3.3. Structural analysis at room temperature from NPD

The crystallographic analysis at room temperature was carried out using neutron powder diffraction data. The crystal structure was successfully refined in the orthorhombic *Cmcm* model from NPD data, reaching an excellent agreement between the observed and calculated patterns, as illustrated in Fig. 4a.

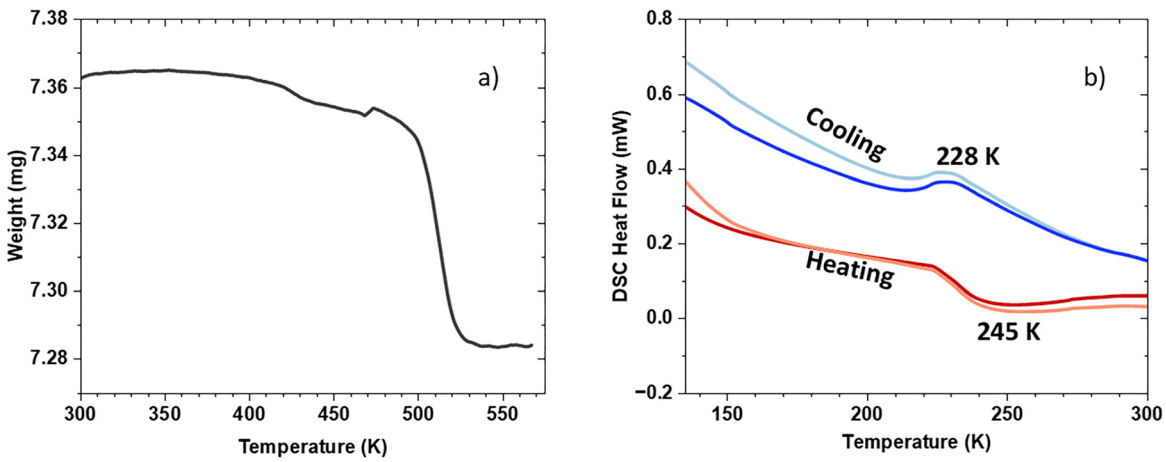

Fig. 2 TG (a) and DSC (b) curves of the $RbCu_2Br_3$ sample in the heating and cooling runs.

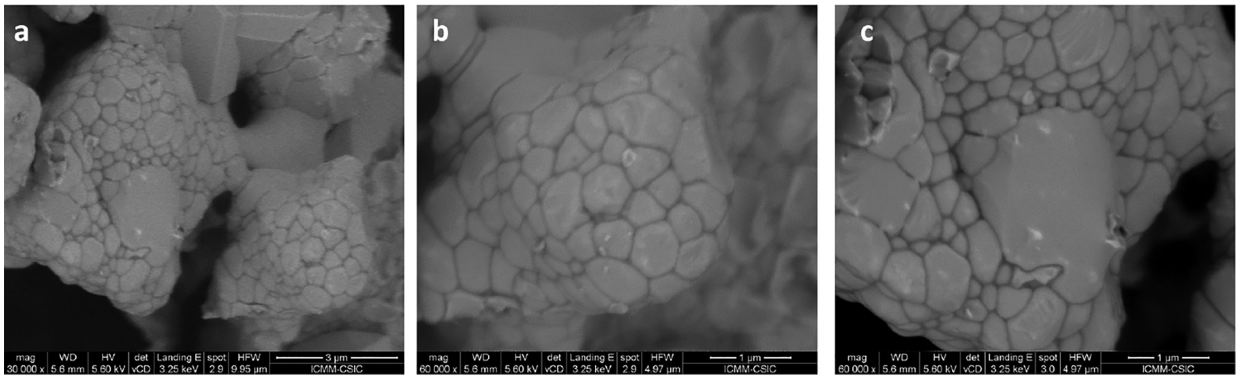

Fig. 3 FE-SEM images of $RbCu_2Br_3$ halides with (b) 30 000×, (b) and (c) 60 000× magnification.

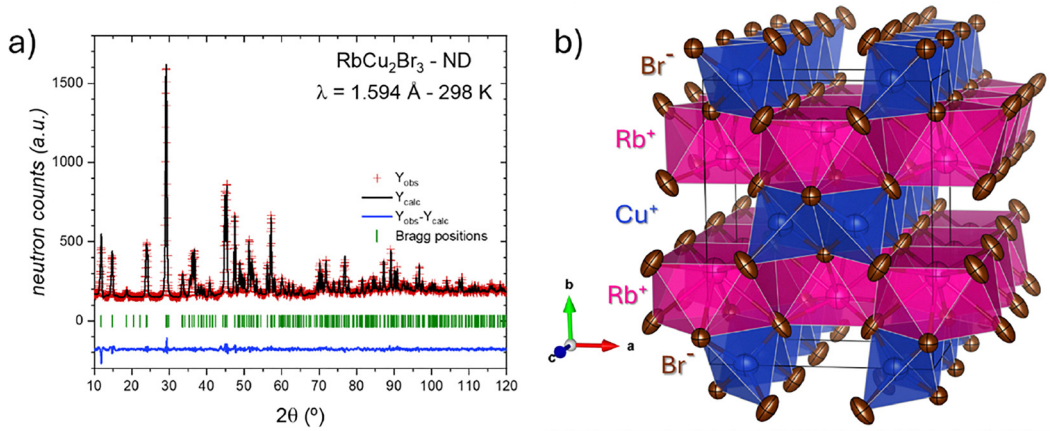

Fig. 4 Rietveld plot: (a) observed (red crosses), calculated (full black line), and difference (blue line) Rietveld profiles for $RbCu_2Br_3$ at 298 K from NPD data. (b) View of the 3D arrangement of $RbCu_2Br_3$ as double chains of edge-sharing $[CuBr_4]$ tetrahedra in the orthorhombic *Cmcm* phase.

The crystal structure comprises $[CuBr_4]$ tetrahedra and $[RbBr_8]$ polyhedra. The $[RbBr_8]$ polyhedra feature ten faces, two square, and eight triangular ones, and are arranged in layers along the *a*–*c* plane, connected *via* their triangular faces. $[CuBr_4]$ tetrahedral units share edges in double chains running along the *c*-axis, linking together the layers of $[RbBr_8]$ polyhedra, as shown in Fig. 4b (Table 1).

3.4. Thermal evolution of crystal structure from SXRD

The synchrotron X-ray powder diffraction method was used to investigate the thermal evolution of the crystal structure in the temperature range 100–530 K. The patterns below room temperature were measured in the ID22 beamline (ESRF, France) at selected temperatures (100, 150, 200, and 250 K). Above 300 K, the patterns were collected sequentially up to 530 K in the MSPD beamline (ALBA, Spain). These patterns were properly refined in the orthorhombic system, showing no evidence of phase transitions. Starting at 510 K, the patterns exhibit a decrease in intensity without significant changes in the unit-cell parameters, which may be attributed to the decomposition of the sample (see Fig. S3). The patterns collected at 530 K and above show no diffraction lines, which agree with a

Table 1 Crystallographic data for $RbCu_2Br_3$ phase in the orthorhombic *Cmcm* space-group from NPD at 298 K. Unit-cell parameters: a = 9.8498(3) Å, b = 12.4032(4) Å, c = 5.5488(1) Å, and V = 677.89(3) Å^3

Atom	Site	x	y	z	U_{eq} (Å^2)	f_{occ}
Rb	4c	0	0.6868(3)	0.250	0.057(2)	1
Cu	8e	0.8337(2)	0	00	0.057(1)	1
Br1	4c	0	0.1172(3)	0.25	0.035(2)	1
Br2	8g	0.7089(2)	0.8751(2)	0.25	0.055(2)	1
Atomic displacement parameters (Å^2)						
Atom	U^{11}	U^{22}	U^{33}	U^{12}	U^{13}	U^{23}
Rb	0.062(2)	0.070(3)	0.040(2)	0	0	0
Cu	0.062(1)	0.063(2)	0.045(1)	0	0	0.012(1)
Br1	0.035(2)	0.037(2)	0.034(2)	0	0	0
Br2	0.054(2)	0.074(2)	0.039(2)	−0.033(1)	0	0

R_p = 2.37%, R_{wp} = 3.05%, χ^2 = 9.35, R_{Bragg} = 5.73%

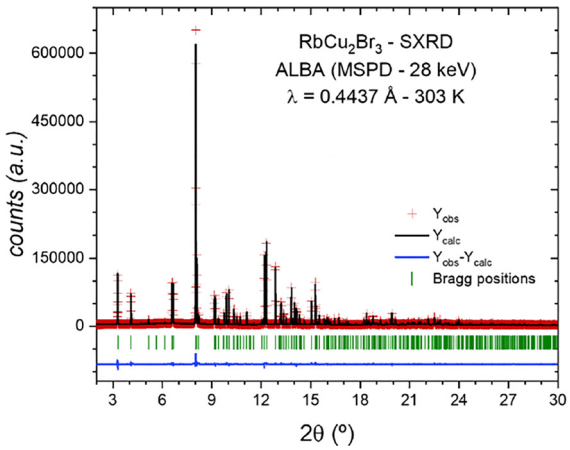

Fig. 5 Rietveld plot: observed (red crosses), calculated (full black line), and difference (blue line) Rietveld profiles for $RbCu_2Br_3$ at 303 K (orthorhombic *Cmcm* phase) from SXRD data.

decomposition process, as it is observed by TG and DSC data. The Rietveld refinement of the SXRD pattern at 303 K is plotted in Fig. 5, and Table S1 lists the main crystallographic data.

The thermal evolution of the SXRD patterns below room temperature exhibits similar features, except for a subtle peak at 5.78° (2θ), which appears in the patterns at 150 and 100 K (Fig. S4). At 200 K, this peak is only incipient and can barely be distinguished from the background. The Rietveld refinement of the four patterns below room temperature unveils an excellent fit with the *Cmcm* space-group at 250 and 200 K, while at 150 and 100 K, the orthorhombic *Pnma* space-group accounts for the additional peaks and provides a superior overall fit. This phase transition was also recently reported by Y. Ding *et al.* from single-crystal XRD data. The Rietveld refinement above and below phase transitions displayed in Fig. 6a and c, respectively, where the inset highlights the (112) diffraction line, which evidences the *Pnma* space-group. Schematic views of both *Cmcm* and *Pnma* symmetries are illustrated in Fig. 6b and d, respectively. Table 2 summarizes the main crystallographic data at 150 K. Table S2 lists the main crystallographic data at 200 K. In Fig. S5 and Fig. S6, the temperature evolution of the lattice parameters and Cu–Br and Rb–Br distances is plotted in the temperature range 100–530 K. It is possible to note that the structural phase transition is produced by a subtle tilt in the [$CuBr_4$] chains along the *b*-axis (in *Pnma* space-group), as discussed later. This transition only involves changes in Rb and Cu positions and an evolution from two to three independent bromine sites in the unit-cell, without changes in the geometries and bonding structure. This observation is consistent with a soft-phase transition, in agreement with the gradual event observed in the DSC measurements. Furthermore, to date, within the isostructural ACu_2X_3 (A = Cs and Rb; X = I, Br, and I) family, evidence of structural phase transition has been found only for $RbCu_2Br_3$. Effectively, for the different ACu_2X_3 halides, the crystal structure is described for all of them in the *Cmcm* orthorhombic space-group ($CsCu_2Cl_3$-type[37]), and no specific reference to a phase transition to *Pnma* is mentioned besides that already mentioned by Ding *et al.*,[31,32] although for $RbCu_2I_3$ an orthorhombic phase is described in the *Pbnm* space-group.[31,32]

3.5. UV-vis diffuse reflectance and photoluminescence spectroscopy

Diffuse-reflectance optical measurements were performed to estimate the optical bandgap of $RbCu_2Br_3$. The spectra were

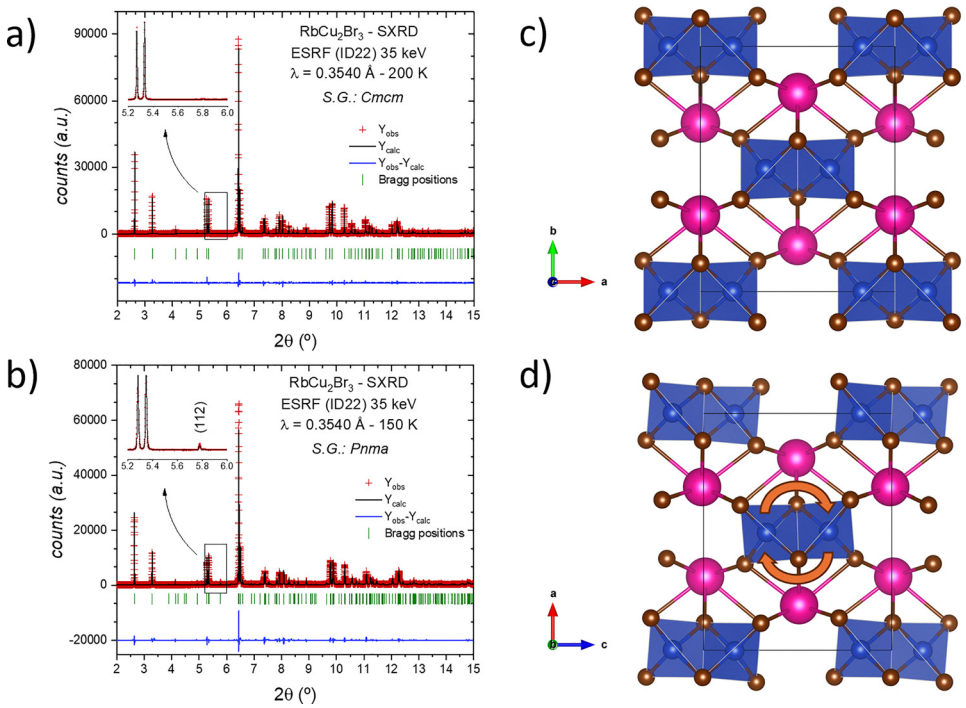

Fig. 6 Rietveld plots of SXRD patterns collected at (a) 200 and (b) 150 K (orthorhombic *Pnma* phase). Insets show a zoom around (112) diffraction line, which reveals the change in the symmetry. Schematic views of crystal structures are exhibited for (c) *Cmcm* and (d) *Pnma* structures.

Table 2 Crystallographic data for $RbCu_2Br_3$ phase in the orthorhombic *Pnma* space-group from SXRD at 150 K. Unit-cell parameters: a = 12.3470(2) Å, b = 5.50569(4) Å, c = 9.8184(1) Å, and V = 667.44(1) Å^3

Atom	Site	x	y	z	U_{eq} (Å^2)	f_{occ}
Rb	4c	0.6892(1)	0.75	−0.0078(4)	0.035(1)	1
Cu	8d	0.4976(2)	0.4979(6)	0.3346(1)	0.037(1)	1
Br1	4c	0.3848(1)	0.25	0.5051(4)	0.018(1)	1
Br2	4c	0.6131(2)	0.25	0.1954(2)	0.036(2)	1
Br3	4c	0.3650(2)	0.75	0.2201(3)	0.024(2)	1
Atomic displacement parameters (Å^2)						
Atom	U^{11}	U^{22}	U^{33}	U^{12}	U^{13}	U^{23}
Rb	0.036(1)	0.040(2)	0.030(1)	0.00000	−0.007(2)	0.00000
Cu	0.036(1)	0.034(1)	0.041(1)	0.008(1)	−0.004(2)	−0.005(3)
Br1	0.0063(1)	0.022(1)	0.027(1)	0.00000	0.005(3)	0.00000
Br2	0.049(2)	0.036(3)	0.024(2)	0.00000	0.024(2)	0.00000
Br3	0.022(2)	0.033(3)	0.018(2)	0.00000	−0.005(2)	0.00000

R_p = 7.7%, R_{wp} = 9.9%, χ^2 = 18.2, R_{Bragg} = 4.10%

converted to Kubelka–Munk (KM) units and analysed using Tauc representations to probe both direct $(h\nu\ \mathrm{KM})^2$ *versus* $h\nu$ and indirect $(h\nu\ \mathrm{KM})^{1/2}$ *versus* $h\nu$ transitions (Fig. 7a). The resulting plots do not allow an unambiguous assignment of the bandgap-type. Nevertheless, a direct transition near ∼3.6 eV is suggested by the higher-energy region, while a lower-energy feature around ∼1.86 eV is consistent with a possible indirect transition. However, a maximum of absorbance associated with localized defect-related states cannot be discarded as it happens with two pronounced features at ∼2.9 and ∼2.2 eV. Additionally, a continuous baseline appears along the KM spectrum, probably due to a small amount of free charge carriers, is the origin of the grey colour of the sample. Localized states and the continuous increase of absorbance *versus* the energy also appear in compounds with

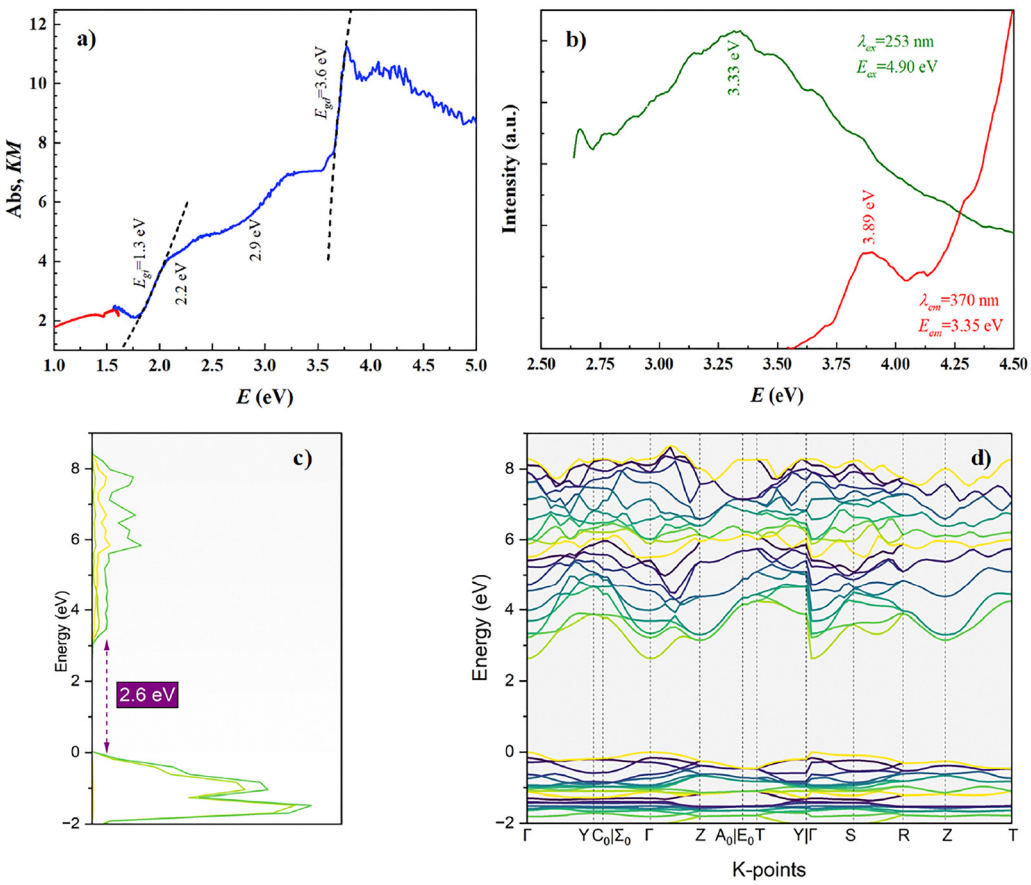

Fig. 7 Tauc plot on visible diffuse reflectance transformed by Kubelka–Munk relationship with the corresponding fittings (dashed lines) to direct (∼3.6 eV) and indirect (∼1.3 eV) bandgaps. (b) Emission due to an excitation at λ_{ex} = 4.90 eV (253 nm) (green line) and excitation measured at λ_{em} = 3.35 eV (370 nm) (red line). Electronic properties of $RbCu_2Br_3$ from DFT calculations. The projected density of states (c) and electronic band structure (d) reveal a direct bandgap of ∼2.6 eV.

cations with several available oxidation states. In this case, a small amount of Cu^{2+} would introduce Cu^{+} or Rb^{+} defects that could explain both features.

Photoluminescence spectra are shown in Fig. 7b. The emission efficiency is poor, probably due to the presence of free carriers, which substantially screens the internal electric field. In any case, emission and excitation peaks, at ~3.33 and ~3.89 eV have been detected. Those features can be explained with an electronic structure with a bandgap of ~3.6 eV, but with many defects. In this regard, emission red shifts due to non-radiative transitions from excitons to localized defects near the conduction band, while excitation, which is like optical absorption, blue shifts from bandgap energy, as the density of states is much larger for higher energies, so that the photon absorption probability is larger from energies slightly higher than that of the bandgap.

To corroborate our experimental findings, theoretical band structure calculations for orthorhombic *Cmcm* $RbCu_2Br_3$ phase were performed within the generalized gradient approximation (GGA) using the Perdew–Burke–Ernzerhof (PBE) exchange correlation functional. Analysis of the projected density of states (p-DOS in Fig. 7c) indicates that the electronic properties are dominated by contributions from Br and Cu orbitals. The valence band maximum is primarily composed of Br orbitals hybridized with Cu orbitals, while the conduction band minimum shows a significant contribution from Br orbitals, with Cu states also participating in the lowest-energy electronic transitions. The calculated band structure, presented in Fig. 7d, reveals a direct band gap of approximately ~2.6 eV at the Γ point of the first Brillouin zone. This value is much lower than the experimentally found value, but this trend is typical for the PBE functional, which is known to underestimate the fundamental bandgap of semiconductors and insulators due to self-interaction errors and the lack of derivative discontinuity in the exchange correlation potential.

3.6. Infrared spectroscopy

While synchrotron X-ray and neutron diffraction techniques give long-range order information (for length ranges larger than ~5 nm), spectroscopy techniques are especially sensitive to short-range ordering.[41–44] In this sense, we carried out near-normal reflectance infrared spectroscopy. This technique allows determining the frequencies, damping, and oscillator strength of infrared optical phonons, especially for isotropic crystals. We deal with a biaxial compound,[45] but, as we have prepared dense cold-sintered pellets, the optical response becomes quasi-isotropic.[46,47] For infrared-active modes with strong oscillator strengths, this approach may not be valid. However, as shown below, the intensities are relatively low; therefore, the isotropization approximation is justified. In Fig. 8, we can see the experimental reflectance spectrum at room temperature with the fitting to a set of oscillators to model the effective dielectric constant $\varepsilon(\omega)$. The relationship between these magnitudes and the near normal reflectance has been carried out by the Fresnel relationships. The first noticeable fact of Fig. 8 is the relatively low value of the maximum of reflectance. These infrared spectra

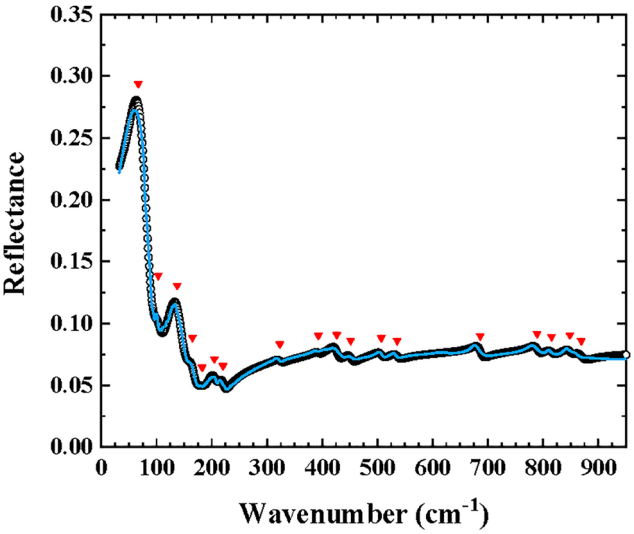

Fig. 8 Near-normal reflectance of a cold-sintered pellet of $RbCu_2Br_3$ (open circles) and fitting (light blue line) at room temperature. Red triangles indicate the transverse frequencies' spectral positions (see Table 3).

Table 3 List of infrared optical modes (transverse ω_T and longitudinal ω_L frequencies), oscillator strength $[1-(\omega_T/\omega_L)^2]$, and damping γ_T of the fitting reflectance spectrum

Mode no.	ω_T (cm^{-1})	ω_L (cm^{-1})	$1-(\omega_T/\omega_L)^2$	γ_T (cm^{-1})
1	67.0	95.9	0.51278	36.0
2	103.3	104.2	0.01720	16.1
3	137.5	146.6	0.11974	35.9
4	165.0	166.4	0.01710	20.0
5	182.7	183.1	0.00470	19.9
6	204.9	205.9	0.00976	19.3
7	220.6	221.0	0.00421	12.2
8	323.4	323.6	0.00116	14.7
9	393.1	393.2	0.00059	12.6
10	426.5	427.3	0.00370	18.0
11	451.7	452.1	0.00196	16.5
12	507.2	507.5	0.00124	15.8
13	536.0	536.3	0.00114	16.9
14	686.3	686.9	0.00176	16.8
15	789.4	789.9	0.00112	17.0
16	815.5	815.9	0.00083	18.5
17	848.6	848.9	0.00074	16.0
18	869.4	870.0	0.00144	23.9

of perovskites display maxima, from the longitudinal to transversal frequencies, very close to unity. The recorded low reflectance values can be related to low values of oscillator strengths (see Table 3), suggesting that the effective charges are minimal and that the metal-halide bonds exhibit only limited ionic character. We have observed up to 18 infrared modes.

The group-theory prediction for the *Cmcm* structure[48,49] determines the following irreducible representation (see Table S3):

$$\Gamma_T = [5A_g \oplus 6B_{1g} \oplus 3B_{2g} \oplus 4B_{3g}]_R \oplus [4B_{1u} \oplus 5B_{2u} \oplus 4B_{3u}]_{IR} \oplus [B_{1u} \oplus B_{2u} + \oplus B_{3u}]_{Ac} \oplus [2A_u]_S$$

These expressions mean that two modes are silent (A_u), 18 are Raman active (A_g, B_{1g}, B_{2g}, B_{3g}), and 13 (B_{1u}, B_{2u}, B_{3u}) are

infrared active. The fact that group-theory predicts fewer modes than those clearly observed implies that the real crystalline structure must have a distortion of the *Cmcm* with fewer symmetry elements.

It should be mentioned that this compound has been reported to present a low-temperature phase with a structure of *Pnma*, as described earlier. Now, considering the *Pnma* structure,[48,49] the group-theory predicts the following (see Table S4):

$$\Gamma_T = [11A_g \oplus 7B_{1g} \oplus 11B_{2g} \oplus 7B_{3g}]_R \oplus [10B_{1u} \oplus 6B_{2u} \oplus 10B_{3u}]_{IR} \oplus [B_{1u} \oplus B_{2u} \oplus B_{3u}]_{Ac} \oplus [7A_u]$$

in this case results in 36 Raman-active, 26 infrared-active, and 7 silent modes. This scheme fits better with the number of modes found in the spectral range analysed. In this context, we cannot rule out the presence of additional infrared modes at frequencies below 50 cm^{-1}, which could not be recorded with our experimental setup.

Reflectance spectrum at 300 K was fitted using the Fresnel formalism,[44,45,50,51] which includes the effective dielectric function $\varepsilon(\omega)$ defined as:

$$\varepsilon(\omega) = \varepsilon_\infty \sum_{k=1}^{N} \frac{\omega_L{}^2 - \omega^2 - i\gamma_L\omega}{\omega_T{}^2 - \omega^2 - i\gamma_T\omega}$$

The parameters of the dielectric function obtained by fitting to near-normal reflectance appear in Table 3, considering 18 infrared modes (dipole oscillators) and in accordance with *Pnma* structural scheme. The infrared frequency modes extend from ~67 to ~870 cm^{-1}, being the ones with the largest intensity, and those with the lowest frequency. We can hypothesize that these modes, ranging from ~67 to ~165 cm^{-1}, are the ones with the largest dipolar component, while the rest of them are due to the breakdown of the symmetry, so that modes with a very low component of dipolar moments arise, but to a very low degree.

4. Discussion

The structural relation between the orthorhombic *Cmcm* (high-symmetry, no. 63) and *Pnma* (low-symmetry, no. 62) phases can be viewed in terms of symmetry-breaking distortions acting on the parent *Cmcm* lattice. Within this framework, the low-symmetry structure is expressed as a linear superposition of the symmetry-adapted distortion modes, each transforming according to a specific irreducible representation (irrep) of the high-symmetry space-group. To construct this decomposition, atomic coordinates in the *Pnma* phase, $r(\mu, i)$ (subgroup H), are referenced to those of the *Cmcm* structure, $r_0(\mu, i)$ (supergroup G), after transforming the latter into the basis of H. The atomic displacements satisfy the following equation:

$$u(\mu, i) = r(\mu, i) - r_0(\mu, i) = \sum_{(\tau,m)} A_{(\tau,m)} \hat{e}_{(\tau,m)}(\mu, i)$$

where μ labels crystallographic sites, $i = 1 \ldots n_\mu$ enumerates the associated atoms, $\hat{e}_{(\tau,m)}$ are the basis vectors of irrep τ, and $A_{(\tau,m)}$ are the corresponding mode amplitudes.

Table 4 Symmetry mode analysis of the $RbCu_2Br_3$ structure showing the site splitting for the low-symmetry structure (*Pnma*) and the symmetry-adapted modes responsible for symmetry lowering from the orthorhombic unit-cell (*Cmcm*). The corresponding amplitudes of the symmetry-adapted modes (normalized within the primitive unit-cell of the high-symmetry structure) are also listed

Cmcm (no. 63)	*Pnma* (no. 62)	Symmetry-adapted modes for each Wyckoff site
Rb1 (4c)	Rb1 (4c)	$\Gamma1^+(1) + Y_2^+(1)$
Cu1 (8e)	Cu1 (8d)	$\Gamma_1^+(1) + Y_2^+(2)$
Br1 (4c)	Br1 (4c)	$\Gamma_1^+(1) + Y_2^+(1)$
Br2 (8g)	Br2–3 (4c)	$\Gamma_1^+(2) + Y_2^+(2)$
Irreps	Γ_1^+	Y_2^+
Direction	(a)	(a)
Dimension	5	6
Amplitude (Å)	0.0876	0.5352
k-vector	(0,0,0)	(1,0,0)
Isotropy group	*Cmcm*	*Pnma*

Such a method was used to identify the amplitudes and polarization vectors of the symmetry-adapted modes that drive the *Cmcm* → *Pnma* transformation. The analysis employed the orthorhombic *Pnma* structure refined at 100 K as the low-symmetry model (see Table S6), together with the *Cmcm* phase refined at 300 K as the high-symmetry model (see Table S5). Both structural models were processed using *Amplimodes*[52] on the *Bilbao Crystallographic Server*[48], ensuring a rigorous decomposition of the structural distortion. Crystallographic data for the 300 K *Cmcm* phase and the transformation matrix (*P*,*p*) relating the two-unit cells are provided in the SI.

Irreps are labelled by their associated *k*-vectors in the first Brillouin zone (here, Γ and Y). The resulting decomposition yields the site splitting listed in Table 4, along with the symmetry-adapted mode amplitudes. This symmetry-resolved analysis establishes the hierarchy and physical character of the distortion modes that stabilize the *Pnma* phase, thereby clarifying the mechanism governing the orthorhombic structural transition.

Site-splitting analysis (Table 4) shows that eleven symmetry-adapted ("frozen") distortion modes are required to describe the orthorhombic distortion of $RbCu_2Br_3$. These modes transform as two irreducible representations (Γ_1^+ and Y_2^+). In the *Cmcm* parent-structure, the Rb1 site (4c) goes into a *Pnma* 4c position, activating two modes [$\Gamma_1^+(1) + Y_2^+(1)$]. The Cu1 site (8e) transforms into the *Pnma* 8d position, giving rise to three modes [$\Gamma_1^+(1) + Y_2^+(2)$]. The Br1 site (4c) also maps onto a *Pnma* 4c position, generating two modes [$\Gamma_1^+(1) + Y_2^+(1)$]. Finally, the Br2 site (8g) splits into two independent positions (Br2 and Br3, both at 4c sites), collectively yielding four modes of identical symmetry [$\Gamma_1^+(2) + Y_2^+(2)$]. Taken together, these distortions constitute a full set of symmetry-adapted modes governing the orthorhombic distortion *Cmcm* → *Pnma* of $Rb_3Cu_2Br_3$.

The symmetry-mode amplitudes summarized in Table 4 unveil that the orthorhombic distortion in $RbCu_2Br_3$ is dominated by the Y_2^+ mode, with an amplitude of ~0.535 Å. This

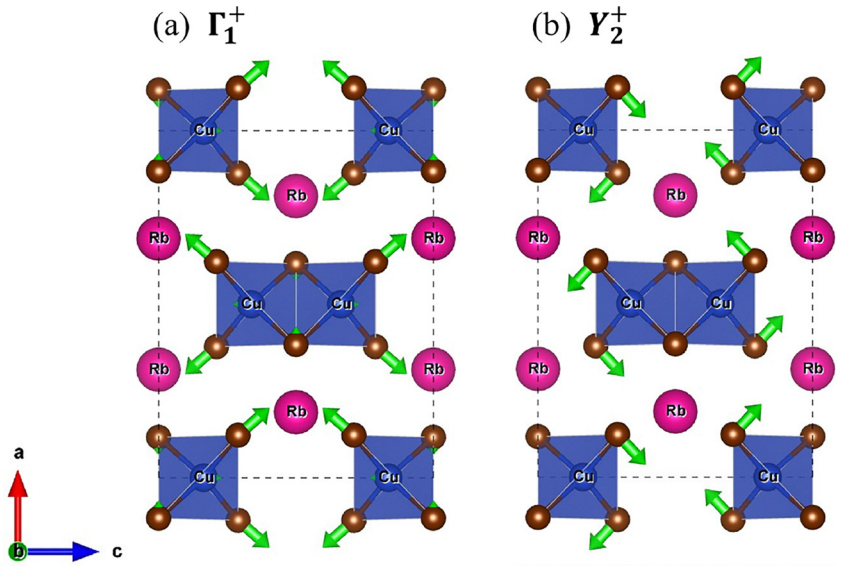

Fig. 9 Atomic displacement patterns for the symmetry-adapted modes involved in the *Cmcm* → *Pnma* transition of $RbCu_2Br_3$. Green arrows denote the direction and relative magnitude of the distortion modes (a) Γ_1^+ and (b) Y_2^+ obtained from the *Amplimodes* analysis. Bromide atoms are shown as brown spheres.

mode corresponds to the cooperative out-of-phase rotations of the $[CuBr_4]$ units, as visualized by the polarization vectors in Fig. 9 and Fig. S7 (where alternative structural perspectives are provided). By contrast, the Γ_1^+ mode (associated with symmetric octahedral stretching) exhibits a much smaller amplitude ($\sim$0.088 Å) and, therefore, plays only a minor role in the orthorhombic distortion. Together, these results indicate that the symmetry lowering accompanying the *Cmcm* → *Pnma* transition is driven predominantly by collective $[CuBr_4]$ tetrahedral-unit rotations.

We can establish that the phase transition in $RbCu_2Br_3$ is best described as a displacive transition driven by the condensation of a collective lattice mode. Although diffraction techniques probe time-averaged atomic positions rather than instantaneous vibrations, the continuous evolution of atomic coordinates and distortion-mode amplitudes provides direct evidence of a frozen-in phonon instability. In particular, the dominant Y_2^+ mode corresponds to a cooperative tilting of the $[CuBr_4]$ chains, involving correlated displacements of Br atoms along the chain direction. As presented, our focus is placed on identifying the microscopic structural mechanism of the *Cmcm* → *Pnma* phase transition in $RbCu_2Br_3$. Through symmetry-adapted mode analysis, the transition is shown to be governed by a single dominant Y_2^+ mode, corresponding to a cooperative tilting of the 1D $[CuBr_4]$ chains. This result provides a clear physical interpretation of the symmetry-breaking and establishes the displacive nature of the transition.

The infrared results at room conditions revealed significantly more active modes than those allowed by the nominal high symmetry *Cmcm* structure, indicating that local symmetry breaking is already present at the short-range scale. Because infrared spectroscopy is highly sensitive to local distortions, the emergence of these additional low-intensity modes (especially those attributed to weak dipolar activity) demonstrates that the structural phase transition begins as a short-range distortion of the $[CuBr_4]$ tetrahedral units. Only at larger length scales, accessible to long-range probes, such as synchrotron X-ray and neutron diffraction, does this distortion fully develop into the long-range *Pnma* ordering. Thus, the combined spectroscopic evidence supports a scenario in which the structural transition nucleates locally and progressively evolves toward long-range coherence, as described by the distortion-mode Y_2^+. While structural distortions of this type are generally expected to influence vibrational and electronic properties through electron–phonon coupling, a quantitative assessment of such effects requires correlations with temperature-dependent spectroscopic data, which are beyond the scope of the present study. The results reported here, therefore, provide a robust structural and symmetry-based framework for understanding the structural phase transition, and serve as a basis for future investigations of structure–property coupling in low-dimensional copper halides.

5. Conclusions

We provide a comprehensive structural and spectroscopic description of the low-dimensional Cu(I) halide $RbCu_2Br_3$, revealing key aspects of its phase stability and lattice dynamics that had remained unresolved. Mechanochemical synthesis yields highly crystalline material without thermal treatment, underscoring the potential of solvent-free routes for preparing metastable or low-dimensional halides. High-resolution neutron and synchrotron X-ray diffraction demonstrate that $RbCu_2Br_3$ is stable in the *Cmcm* phase at room temperature but undergoes a soft, symmetry-lowering transition to *Pnma* below $\sim$250 K. This transition is governed by low-amplitude,

symmetry-adapted distortions dominated by cooperative [$CuBr_4$] chain tilting, and involves minimal modification of local coordination environments, in agreement with calorimetric hysteresis and the emergence of additional diffraction peaks. Infrared spectroscopy reveals an unexpectedly rich phonon spectrum arising from local symmetry breaking and the weakly ionic character of Cu–Br bonds, complementing the long-range structural picture provided by diffraction data. Optical diffuse reflectance, photoluminescence, and DFT calculations jointly confirm the presence of both direct and indirect electronic transitions, linked to hybridized Cu–Br states that define the electronic frontier levels. Overall, $RbCu_2Br_3$ emerges as a structurally flexible, low-dimensional, lead-free halide whose lattice is highly susceptible to symmetry-lowering instabilities. These results not only clarify the microscopic mechanism of its low-temperature transformation but also position this family of Cu(I)-based halides as promising platforms for exploring structure–property coupling, excitonic behaviour, and potential optoelectronic functionality in environmentally benign materials.

Author contributions

YC, JG, and JEFSR synthesized the samples. FSS, JG, and LK carried out thermal analysis and microscopy. CAL, FSS, MTFD, JEFSR, and JAA performed and analysed the structural data. BM and MMF carried out the DFT calculations. JLM, WC, JEFSR, and JAA conceived the study. CP and JEFSR performed and analysed the optical data. JLM and JAA obtained the funding. All the authors participated in discussing the results and commented on the manuscript.

Conflicts of interest

There are no conflicts to declare.

Data availability

Neutron data described in this article are available at the Institut Laue Langevin (ILL) repository, at DOI: https://doi.org/10.5291/ILL-DATA.5-24-707. Synchrotron X-ray diffraction data collected at ID22 during experiment HC-5818 are available at the ESRF repository, at DOI: https://doi.esrf.fr/10.15151/ESRF-ES-1911533009. Embargo periods may apply.

Supplementary information (SI): chemical and morphological analyses of $RbCu_2Br_3$ in Fig. S1 and S2. Raw temperature-dependent SXRD in Fig. S3 and S4. The temperature evolution of the lattice parameters and Cu–Br and Rb–Br distances in Fig. S5 and S6. Crystallographic data for $RbCu_2Br_3$ phase in the orthorhombic *Cmcm* space-group at 303 and 200 K in Tables S1 and S2. Factor-group analysis for the *Cmcm* and *Pnma* structures in Tables S3 and S4. Alternative view of the atomic displacement patterns for the symmetry-adapted modes of $RbCu_2Br_3$ in Fig. S7. Crystallographic data employed for distortion-mode analysis in Table S5 and Table S6. See DOI: https://doi.org/10.1039/d5tc04105h.

Acknowledgements

We acknowledge the financial support of the Spanish Ministry for Science and Innovation (MCIN/AEI/10.13039/501100011033) for granting the projects: PID2021-122477OB-I00, TED2021-129254B-C21, and TED2021-129254B-C22. CAL acknowledges UNSL, CONICET, and ANPCyT for financial support (projects PROICO 2-2320; PIP2972 and PICT2020A-2437, respectively). This work was supported by Fundação de Amparo à Pesquisa do Estado do Rio Grande do Sul [FAPERGS, Grant 23/2551-0000153-5], Conselho Nacional de Desenvolvimento Científico e Tecnológico [CNPq, Grants 406160/2023-6, 307213/2021-8, 150187/2023-8, and 314278/2023-0], and Fundação de Amparo à Pesquisa do Estado de São Paulo [FAPESP, Grants 22/03959-6, 22/16509-9, and 20/01144-0]. The authors wish to express their gratitude to ALBA, ESRF, and ILL technical staff for making the facilities available for the synchrotron X-ray and neutron powder diffraction experiments.

References

1 J. Y. Kim, J.-W. Lee, H. S. Jung, H. Shin and N.-G. Park, *Chem. Rev.*, 2020, **120**, 7867–7918.
2 W. Lv, L. Li, M. Xu, J. Hong, X. Tang, L. Xu, Y. Wu, R. Zhu, R. Chen and W. Huang, *Adv. Mater.*, 2019, **31**(28), 1900682.
3 E. M. Hutter, G. E. Eperon, S. D. Stranks and T. J. Savenije, *J. Phys. Chem. Lett.*, 2015, **6**, 3082–3090.
4 D. Cortecchia, J. Yin, A. Petrozza and C. Soci, *J. Mater. Chem. C*, 2019, **7**, 4956–4969.
5 T. He, Y. Jiang, X. Xing and M. Yuan, *Adv. Mater.*, 2020, **32**(26), 1903937.
6 Y. Park, M.-K. Kim and J.-S. Lee, *J. Mater. Chem. C*, 2021, **9**, 1429–1436.
7 F. P. García de Arquer, A. Armin, P. Meredith and E. H. Sargent, *Nat. Rev. Mater.*, 2017, **2**, 16100.
8 C. Bao, J. Yang, S. Bai, W. Xu, Z. Yan, Q. Xu, J. Liu, W. Zhang and F. Gao, *Adv. Mater.*, 2018, **30**(38), 1803422.
9 J. Feng, C. Gong, H. Gao, W. Wen, Y. Gong, X. Jiang, B. Zhang, Y. Wu, Y. Wu, H. Fu, L. Jiang and X. Zhang, *Nat. Electron.*, 2018, **1**, 404–410.
10 J. Wang, J. Wang, N. Li, X. Du, J. Ma, C. He and Z. Li, *ACS Appl. Mater. Interfaces*, 2020, **12**, 31477–31485.
11 Z. Hong, W. K. Chong, A. Y. R. Ng, M. Li, R. Ganguly, T. C. Sum and H. Sen Soo, *Angew. Chem., Int. Ed.*, 2019, **58**, 3456–3460.
12 K. Ren, S. Yue, C. Li, Z. Fang, K. A. M. Gasem, J. Leszczynski, S. Qu, Z. Wang and M. Fan, *J. Mater. Chem. A*, 2022, **10**, 407–429.
13 Q. Zhang, Q. Shang, R. Su, T. T. H. Do and Q. Xiong, *Nano Lett.*, 2021, **21**, 1903–1914.
14 S. Das, S. Gholipour and M. Saliba, *Energy Environ. Mater.*, 2019, **2**, 146–153.

15 J. Liu, B. Shabbir, C. Wang, T. Wan, Q. Ou, P. Yu, A. Tadich, X. Jiao, D. Chu, D. Qi, D. Li, R. Kan, Y. Huang, Y. Dong, J. Jasieniak, Y. Zhang and Q. Bao, *Adv. Mater.*, 2019, **31**(30), 1901644.
16 S. Deumel, A. van Breemen, G. Gelinck, B. Peeters, J. Maas, R. Verbeek, S. Shanmugam, H. Akkerman, E. Meulenkamp, J. E. Huerdler, M. Acharya, M. García-Batlle, O. Almora, A. Guerrero, G. Garcia-Belmonte, W. Heiss, O. Schmidt and S. F. Tedde, *Nat. Electron.*, 2021, **4**, 681–688.
17 H. Zhang, Z. Yang, M. Zhou, L. Zhao, T. Jiang, H. Yang, X. Yu, J. Qiu, Y. (Michael) Yang and X. Xu, *Adv. Mater.*, 2021, **33**(40), 2102529.
18 T. Xia, Y. Li, L. Huang, W. Ji, M. Yang and X. Zhao, *ACS Appl. Mater. Interfaces*, 2020, **12**, 18634–18641.
19 A. Swarnkar, A. R. Marshall, E. M. Sanehira, B. D. Chernomordik, D. T. Moore, J. A. Christians, T. Chakrabarti and J. M. Luther, *Science*, 2016, **354**, 92–95.
20 Y. Wang, M. I. Dar, L. K. Ono, T. Zhang, M. Kan, Y. Li, L. Zhang, X. Wang, Y. Yang, X. Gao, Y. Qi, M. Grätzel and Y. Zhao, *Science*, 2019, **365**, 591–595.
21 K. Lin, J. Xing, L. N. Quan, F. P. G. de Arquer, X. Gong, J. Lu, L. Xie, W. Zhao, D. Zhang, C. Yan, W. Li, X. Liu, Y. Lu, J. Kirman, E. H. Sargent, Q. Xiong and Z. Wei, *Nature*, 2018, **562**, 245–248.
22 C. A. López, C. Abia, M. C. Alvarez-Galván, B.-K. Hong, M. V. Martínez-Huerta, F. Serrano-Sánchez, F. Carrascoso, A. Castellanos-Gómez, M. T. Fernández-Díaz and J. A. Alonso, *ACS Omega*, 2020, **5**, 5931–5938.
23 D. Han, J. Wang, L. Agosta, Z. Zang, B. Zhao, L. Kong, H. Lu, I. Mosquera-Lois, V. Carnevali, J. Dong, J. Zhou, H. Ji, L. Pfeifer, S. M. Zakeeruddin, Y. Yang, B. Wu, U. Rothlisberger, X. Yang, M. Grätzel and N. Wang, *Nature*, 2024, **632**, E5–E5.
24 A. H. Slavney, T. Hu, A. M. Lindenberg and H. I. Karunadasa, *J. Am. Chem. Soc.*, 2016, **138**, 2138–2141.
25 S. F. Hoefler, G. Trimmel and T. Rath, *Monatsh. Chem.*, 2017, **148**, 795–826.
26 J. E. F. S. Rodrigues, C. A. Escanhoela, B. Fragoso, G. Sombrio, M. M. Ferrer, C. Álvarez-Galván, M. T. Fernández-Díaz, J. A. Souza, F. F. Ferreira, C. Pecharromán and J. A. Alonso, *Ind. Eng. Chem. Res.*, 2021, **60**, 18918–18928.
27 E. Greul, M. L. Petrus, A. Binek, P. Docampo and T. Bein, *J. Mater. Chem. A*, 2017, **5**, 19972–19981.
28 F. Bai, Y. Hu, Y. Hu, T. Qiu, X. Miao and S. Zhang, *Sol. Energy Mater. Sol. Cells*, 2018, **184**, 15–21.
29 T. Jun, K. Sim, S. Iimura, M. Sasase, H. Kamioka, J. Kim and H. Hosono, *Adv. Mater.*, 2018, **30**(43), 1804547.
30 B. Yang, L. Yin, G. Niu, J. Yuan, K. Xue, Z. Tan, X. Miao, M. Niu, X. Du, H. Song, E. Lifshitz and J. Tang, *Adv. Mater.*, 2019, **31**(44), 1904711.
31 Y. Ding, R. Lin, S. Zhu, Z. Lin and W. Zheng, *Adv. Opt. Mater.*, 2023, **11**(13), 2202730.
32 Y. Ding, R. Lin, Z. Lin and W. Zheng, *J. Mater. Chem. C*, 2023, **11**, 2531–2539.
33 S. Hull and P. Berastegui, *J. Solid State Chem.*, 2004, **177**, 3156–3173.
34 A. Fitch, C. Dejoie, E. Covacci, G. Confalonieri, O. Grendal, L. Claustre, P. Guillou, J. Kieffer, W. de Nolf, S. Petitdemange, M. Ruat and Y. Watier, *J. Synchrotron Radiat.*, 2023, **30**, 1–10.
35 F. Fauth, R. Boer, F. Gil-Ortiz, C. Popescu, O. Vallcorba, I. Peral, D. Fullà, J. Benach and J. Juanhuix, *Eur. Phys. J. Plus*, 2015, **130**, 160.
36 J. Rodríguez-Carvajal, *Phys. B Phys. Condens. Matter*, 1993, **192**, 55–69.
37 A. Wojakowska, E. Krzyżak and A. Wojakowski, *J. Therm. Anal. Calorim.*, 2001, **65**, 491–495.
38 A. Erba, J. K. Desmarais, S. Casassa, B. Civalleri, L. Donà, I. J. Bush, B. Searle, L. Maschio, L. Edith-Daga, A. Cossard, C. Ribaldone, E. Ascrizzi, N. L. Marana, J. P. Flament and B. Kirtman, *J. Chem. Theory Comput.*, 2023, **19**, 6891–6932.
39 J. P. Perdew, A. Ruzsinszky, G. I. Csonka, O. A. Vydrov, G. E. Scuseria, L. A. Constantin, X. Zhou and K. Burke, *Phys. Rev. Lett.*, 2008, **100**, 136406.
40 J. Laun, D. Vilela Oliveira and T. Bredow, *J. Comput. Chem.*, 2018, **39**, 1285–1290.
41 H. Kuzmany, *Solid-State Spectroscopy: An Introduction*, *Springer Berlin Heidelberg*, 2013.
42 D. A. Long, *The Raman Effect: A Unified Treatment of the Theory of Raman Scattering by Molecules*, John Wiley & Sons, West Sussex, England, 2002.
43 P. A. Lee, P. H. Citrin, P. Eisenberger and B. M. Kincaid, *Rev. Mod. Phys.*, 1981, **53**, 769–806.
44 C. Pecharromán, M. Ocaña and C. J. Sema, *J. Appl. Phys.*, 1996, **80**, 3479–3483.
45 J. E. F. S. Rodrigues, M. M. Ferrer, M. L. Moreira, J. R. Sambrano, R. C. Costa, A. D. Rodrigues, P. S. Pizani, Y. Huttel, J. A. Alonso and C. Pecharromán, *J. Alloys Compd.*, 2020, **813**, 152136.
46 C. Pecharroman and J. E. Iglesias, *J. Phys.: Condens. Matter*, 1994, **6**, 7125–7141.
47 C. Pecharromán, T. González-Carreño and J. E. Iglesias, *J. Mater. Res.*, 1996, **11**, 127–133.
48 E. Kroumova, M. I. Aroyo, J. M. Perez-Mato, A. Kirov, C. Capillas, S. Ivantchev and H. Wondratschek, *Phase Transitions*, 2003, **76**, 155–170.
49 D. L. Rousseau, R. P. Bauman and S. P. S. Porto, *J. Raman Spectrosc.*, 1981, **10**, 253–290.
50 C. Pecharromán, F. Gracía, J. P. Holgado, M. Ocaña, A. R. González-Elipe, J. Bassas, J. Santiso and A. Figueras, *J. Appl. Phys.*, 2003, **93**, 4634–4645.
51 C. Pecharromán and J. E. Iglesias, *Appl. Spectrosc.*, 2000, **54**, 634–638.
52 J. M. Perez-Mato, D. Orobengoa and M. I. Aroyo, *Mode crystallography of distorted structures*, International Union of Crystallography, 2010, vol. 66.